Very long wavelength infrared focal plane arrays with 50% cutoff wavelength based on type-II InAs/GaSb superlattice*

Xi Han(韩玺)[1,2], Wei Xiang(向伟)[1,2], Hong-Yue Hao(郝宏玥)[1,2], Dong-Wei Jiang(蒋洞微)[1,2], Yao-Yao Sun(孙姚耀)[1,2], Guo-Wei Wang(王国伟)[1,2], Ying-Qiang Xu(徐应强)[1,2], and Zhi-Chuan Niu(牛智川)[1,2,†]

[1] *State Key Laboratory for Superlattices and Microstructures, Institute of Semiconductors, Chinese Academy of Sciences, Beijing* 100083, *China*
[2] *Synergetic Innovation Centre of Quantum Information and Quantum Physics, University of Science and Technology of China, Hefei* 230026, *China*

(Received 18 July 2016; revised manuscript received 18 October 2016; published online 10 December 2016)

A very long wavelength infrared(VLWIR) focal plane array based on InAs/GaSb type-II super-lattices is demonstrated on a GaSb substrate. A hetero-structure photodiode was grown with a 50% cut-off wavelength of 15.2 μm, at 77 K. A 320×256 VLWIR focal plane array with this design was fabricated and characterized. The peak quantum efficiency without an antireflective coating was 25.74% at the reverse bias voltage of −20 mV, yielding a peak specific detectivity of 5.89×10^{10} cm·Hz$^{1/2}$·W^{-1}. The operability and the uniformity of response were 89% and 83.17%. The noise-equivalent temperature difference at 65 K exhibited a minimum at 21.4 mK, corresponding to an average value of 56.3 mK.

Keywords: very long wavelength infrared, type-II InAs/GaSb super-lattices (T2SLs), focal plane array

PACS: 85.60.Gz, 73.21.Cd, 73.40.Kp **DOI:** 10.1088/1674-1056/26/1/018505

1. Introduction

Since the introduction of type-II InAs/GaSb super-lattices (T2SLs) by Esaki and Tsu in the late 1970s,[1] T2SLs have attracted considerable interest for infrared (IR) photo-detection, owing to their low Auger recombination rate, relatively long carrier lifetime, flexible tuning of the detection wavelength, and good material uniformity. The first reports of detection devices with promising electro-optical properties[2,3] appeared in the 1990s. Further progress in band structure modelling,[4] material quality,[5] and fabrication and testing[6,7] has been made, suggesting T2SLs as a viable alternative to mercury–cadmium–telluride (MCT) material systems that dominate the current market of IR detectors, especially for detecting long wavelength infrared (LWIR) and very long wavelength infrared (VLWIR) radiation.

Significant progress has been made in the field of focal plane arrays (FPAs) based on InAs/GaSb T2SLs, from mid wavelength IR to LWIR.[8–10] Compared with short wavelength and mid-wavelength IR detectors, the bandgap of VLWIR detectors is very narrow, especially for wavelengths longer than 12 μm. In the fabrication of T2SL VLWIR FPAs, the biggest problem is a relatively strong dark current and a relatively low differential resistance area product at zero bias (R_0A), which limits the ability to match readout integrated circuits.[11] Achieving high R_0A requires using high-quality materials, optimising the device's energy structure, and proper processing and passivation. Besides, quantum efficiency (QE)[12] is another important parameter for characterising the detector performance.

In this paper, we present an integrated process of fabricating VLWIR FPAs. Firstly, an optimised strain balance process was used to precisely control the molecular beam epitaxy (MBE) growth parameters for VLWIR SL materials. To balance the larger tensile stress owing to the thicker InAs layers, we used a double-InSb-like surface and an additional thin GaInSb layer that was inserted between the GaSb layers.[13] This design reduced the difficulties associated with the material growth and improved the quality of the wafers. Secondly, a properly doped M barrier was inserted between the active region and the N contact region. It was reported that an M structure super-lattice can be used as a barrier for spatially separating the tunnelling channel and reducing both the tunnelling and diffusion currents, owing to a large effective mass in the M structure layers.[14–16] Thirdly, a proper dry etching process was designed for etching the FPAs mesa after photolithography. The devices were passivatedusing both chemical passivation based on the anode sulphide and physical passivation using the material SiO_2. The FPA device was characterised after the metal and indium bump deposition and flip-chip bonding.

2. Experimental methods

2.1. Material structure and characterisation

The materials in this study were grown using a GEN II molecular beam epitaxy (MBE) system on a 2-inch-thick GaSb wafer. A detailed description of the growth process was provided elsewhere.[17] The growth started with a ∼0.75-μm-

*Project supported by the National Basic Research Program of China (Grant Nos. 2013CB932904 and 2011CB922201), the National Special Funds for the Development of Major Research Equipment and Instruments, China (Grant No. 2012YQ140005), and the National Natural Science Foundation of China (Grant Nos. 61274013, 61290303, and 61306013).

†Corresponding author. E-mail: zcniu@semi.ac.cn

© 2017 Chinese Physical Society and IOP Publishing Ltd

thick GaSb:Be p+ ($p \sim 10^{18}$ cm^{-3}) buffer layer; a 0.69-μm-thick P contact layer, consisting of 8 InAs monolayers and 12 GaSb monolayers doped with Be p+ ($p \sim 10^{18}$ cm^{-3}); a 1.5-μm-thick active layer, consisting of 15 InAs monolayers/3.5 GaSb monolayers/0.6 InSb monolayers/3.5 GaSb monolayers, lightly doped with Be at 760 °C in the InAs layers and during the last 50 periods gradually doped from 760 °C to 740 °C at a rate of 10 °C/min; a 0.5-μm-thick M structure super-lattice, consisting of 18 InAs monolayers/3 GaSb monolayers/5 AlSb monolayers/3 GaSb monolayers, lightly doped with Si by keeping the Si dopant cell at 1080 °C; a 0.5-μm-thick N contact layer, the structure of which was the same as that of the M structure except the Si dopant at 1240 °C; and an InAs:Si ($n \sim 10^{18}$ cm^{-3}) layer. Gradual doping was achieved by changing the Si doping temperature from 1080 °C to 1240 °C at a rate of 20 °C/min, during the first 20 periods in the N contact region.

The device is schematically shown in Fig. 1(a). Material quality was characterised using high-resolution x-ray diffraction (HRXRD) and atomic force microscopy (AFM). Figure 1(b) shows the AFM image of a typical 20×20 μm^2 area. The surface morphology measurements revealed long atomic steps with a root mean square (RMS) surface roughness of 1.43 Å over an area of 10×10 μm^2. In addition, in a larger surface scan (20×20 μm^2), only a few growth defects were detected, suggesting a satisfactory surface morphology. The HRXRD patterns in Fig. 1(c) exhibit super-lattice periods of 62.9 Å, 71.5 Å, and 89.9 Å for the p-contact, p-active region, and M-structure layer, with lattice mismatches of 0 arcsec, 0 arcsec, and 185.8 arcsec, respectively. The full width at half maximum (FWHM) for the SLs in different regions were 19.8 arcsec, 16.1 arcsec, and 29.3 arcsec, indicating high-quality material at the interfaces.

2.2. Device fabrication

Next, we fabricated the FPA device. The wafers were covered with SiO_2 as a hard etching mask, and patterned using standard ultraviolet (UV) photolithography. After defining the mesas by etching the SiO_2 mask, the wafers were etched through the cap layer and the super-lattice layers and into the GaSb buffer layer, using an inductively-coupled plasma (ICP) system with a $CH_4/Cl_4/Ar_2$ mixture. After removing residual SiO_2, the arrays were passivated by the anodic sulphide as a chemical passivation, to fill the dangling bonds on the surface. A 200-nm-thick layer of SiO_2 was deposited using ion beam sputtering deposition (IBSD) as the physical passivation. Next, photolithography was again performed to open the windows through the passivation layer as the metal contact regions, where the top and bottom metal electrodes were formed using the electron-beam-deposited Ti (500 Å)/Pt (500 Å)/Au (3000 Å). After depositing a tall indium bumpand flip-chip bonding, the VLWIR array was brought in contact with a readout integrated circuit (ROIC). Careful attention was paid to clean the wafers throughout the entire processing step, to reduce the risk of contamination on the pixel sidewalls. The above processes were also reported previously.[18] Final substrate thinning was performed as a last step,[19] to reduce the absorption by the substrate and antireflection (AR) coating for high-performance imaging. The fabricated FPAs consisted of 320×256 pixels with a 30×30 μm^2 pitch. A linear array close to the FPAs on the wafer was fabricated at the same time.

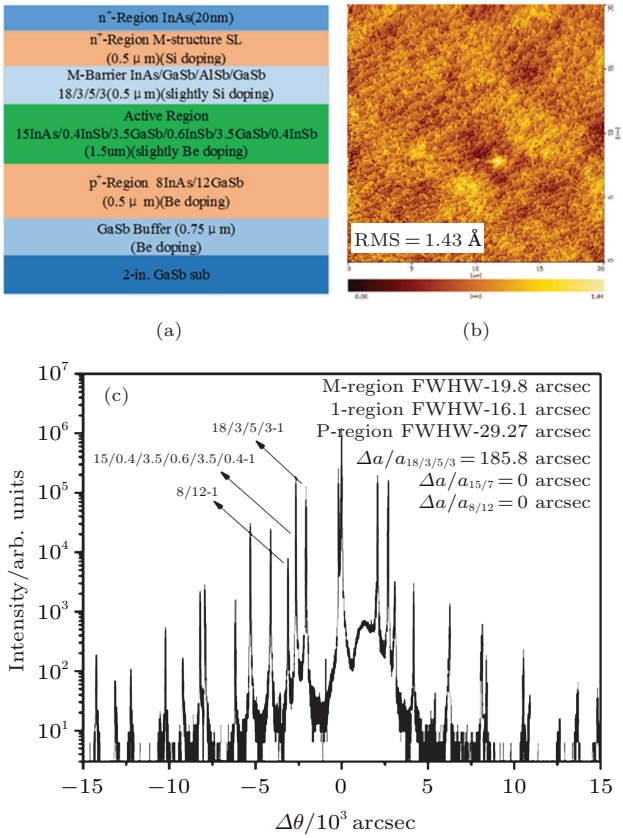


Fig. 1. (color online) (a) Schematic of the N-M-π-P detector heterostructure. (b) AFM image of a typical 20×20 μm^2 area. (c) High-resolution x-ray diffraction spectrum and characterization according to different super-lattices.

3. Results and discussion

3.1. *I–V* characterisation

Measurements of electrical characteristics were performed on a single element device in a linear array 27×27 μm^2 array, at temperatures ranging from 50 K to 77 K. Figure 2 shows the dark current density curves and the differential resistance area product curves of the diodes in the linear array. The maximal RA product values for 55 K and 77 K were 0.0517 Ω·cm^2 (obtained at the reverse bias voltage of −44 mV) and 0.0339 Ω·cm^2 (obtained at the reverse bias voltage of −52 mV), respectively. Figure 2(a) shows that the *J–V* curves for different temperatures are similar for the reverse bias voltage above 100 mV, indicating that the device oper-

ates in a tunnelling dark current mode that relatively weakly depends on the temperature. However, for low reverse bias voltages, especially below 80 mV, the dark current exhibits a stronger dependence on the temperature, increasing with increasing temperature, which indicates that a different current mechanism is dominant in this regime, e.g., generation–recombination (G–R).

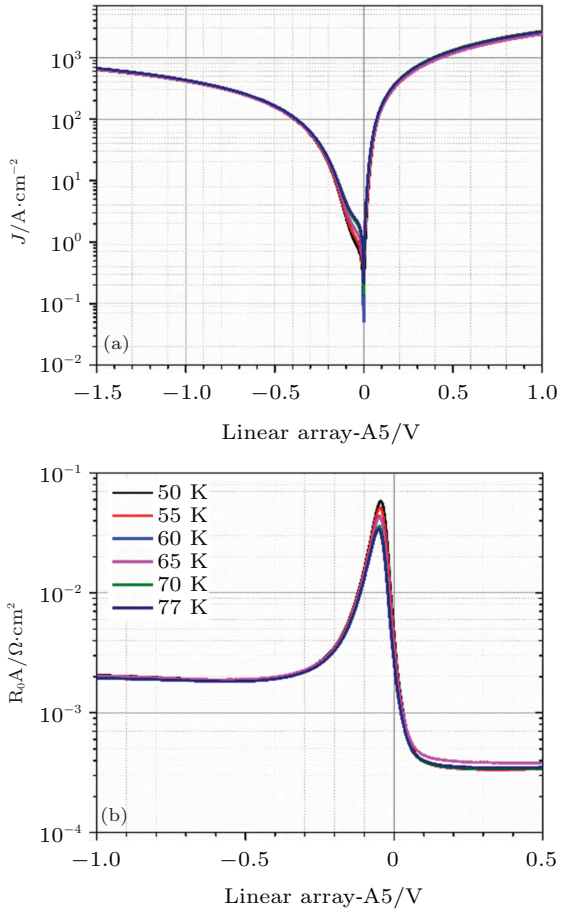


Fig. 2. (color online) Single element device characterization. (a) Current density vs. voltage. (b) Differential resistance vs. voltage.

To investigate the mechanism of the dark current for the fabricated array further, the R_0A product was measured as a function of temperature, offering insights on the dark current mechanism in individual elements. Figure 3 shows the R_0A values for two elements in a linear array, versus the inverse of the temperature, for temperatures in the 10–200 K range, measured for a 7.29×10^{-6} cm^2 area. In Fig. 3, the elements are labelled as A4 and A5, corresponding to their different locations in the wafer. Although all mechanisms become more pronounced with increasing temperature, the dependences are not the same, resulting in the variation in the dominant mechanism with temperature across elemental devices. Because diffusion exhibits the strongest dependence on temperature, it is the most dominant mechanism at high temperatures, and R_0A decreases rapidly with increasing temperature. From 50 K to 100 K, the dark current decreases slower than that in the high-temperature regime, and it is more likely that G–R is the dominant mechanism. As the temperature decreases further, both the diffusion and G–R currents become smaller and are eventually overshadowed by tunnelling and surface leakage currents. From the results in Fig. 3, the surface leakage current becomes dominant for temperatures in the 30–45 K range. In the 10–30 K range, the tunnelling current is the dominant mechanism, which is manifested as a relatively flat temperature dependence.

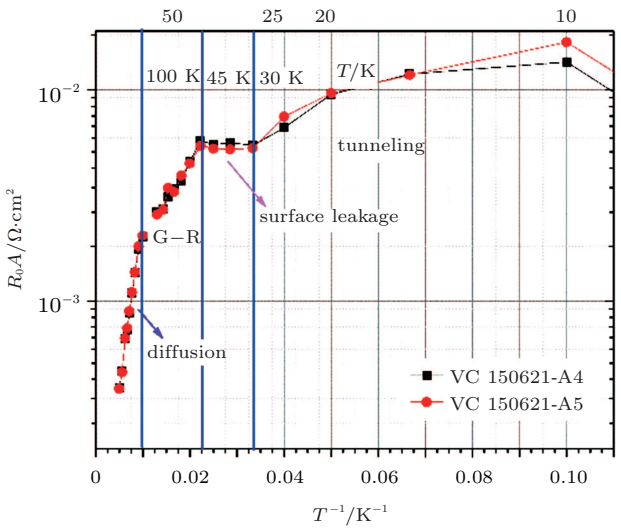


Fig. 3. (color online) R_0A vs. the inverse of temperature.

3.2. Spectral response

Optical characterisation of single diodes was performed at 77 K using a Fourier transform infrared (FTIR) spectrometer and a calibrated blackbody source at the temperature of 500 K. Figure 4(a) shows the quantum efficiency as a function of wavelength, measured using the detector at different bias voltages. The QE increases as the positive bias voltage decreases from 25 mV to 0 mV. As the reverse bias voltage increases from 0 mV to −100 mV, the QE first increases and then decreases. The maximal QE is ∼25.74%, obtained for the bias voltage of −20 mV, and the relevant wavelength is 11.9 μm. The small applied reverse bias voltage is owing to the proper doping level in the M barrier region. Besides, the elements exhibit a 50% cutoff wavelength of 15.2 μm and a 100% cutoff wavelength of nearly 18.5 μm. For a T2SL IR detector with a ∼ 1.5-μm-thick active region, the QE was demonstrated to reach the potential maximal value without anti-reflecting coating.[20] The relatively high QE can be attributed to the proper gradual doping and absorption in the device structure and to the introduction of a double-InSb-like interface. Gradual doping extended the electron diffusion length and increased the absorption coefficient. The double-InSb-like interface likely also contributed to increasing the material's absorption coefficient. The QE could be further im-

proved by increasing the thickness of the active region. Figure 4(b) shows the calculated specific detectivity of the elements, for different bias voltages. The maximal detectivity was 5.89×10^{10} cm·Hz$^{1/2}$·W^{-1}, and it was obtained for −50 mV.

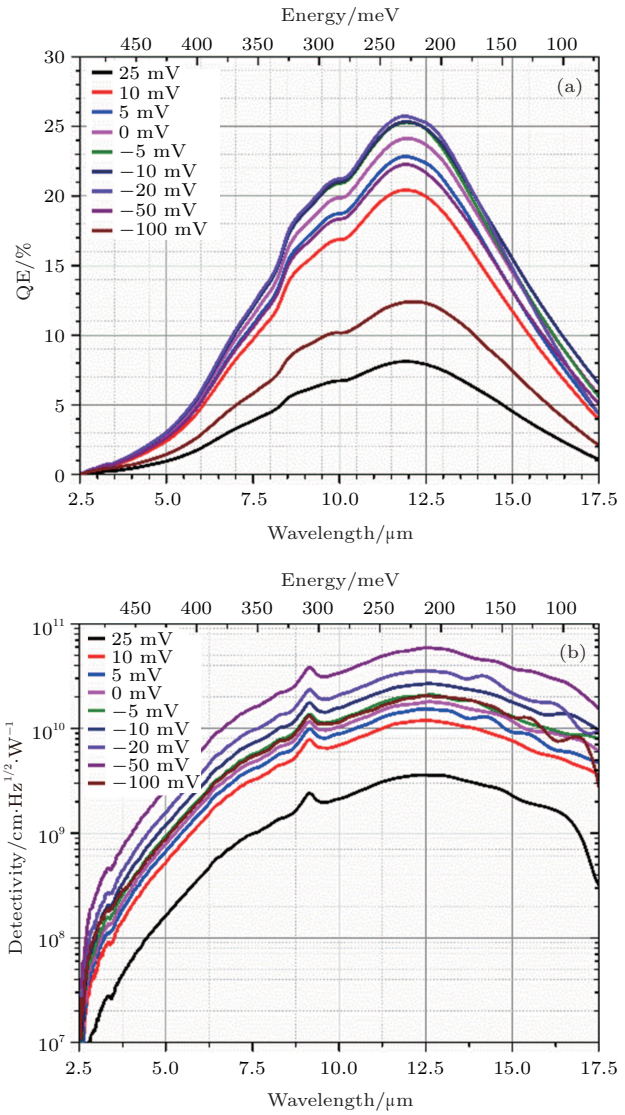


Fig. 4. (color online) Spectral elemental responses, measured at 77 K. (a) Quantum efficiency. (b) Specific detectivity.

3.3. Focal plane array

The VLWIR FPAs were tested at 65 K and a thermal image was acquired using a 320×256 FPA camera and is shown in Fig. 5(a). A pixel was defined as operable if its noise was lower than twice the noise of the median pixel and its responsivity was within 50% of the responsivity of the median pixel. The non-uniformity U was calculated as the standard deviation σ of a quantity over the mean value of the same quantity calculated on only the operating pixels, $U = \sigma$/mean. The operability and uniformity of responsivity were 89% and 83.17%, respectively. Compared with the previously reported MWIR and LWIR FPAs,[8,21] the operability and uniformity are not satisfactory. However, they can be further improved by optimizing the fabrication steps and the quality of the wafers. Figure 5(b) shows the responsivity of the array.

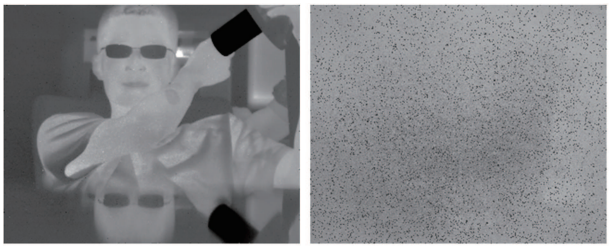


Fig. 5. (color online) A thermal image, acquired using a 320×256 VLWIR FPA at 65 K, and a mirror image reflected by a desk located in front of the researcher. (b)Responsivity of the array at 65 K.

The equivalent temperature difference (NEDT) was measured using an extended blackbody source with the target temperature varying between 25 °C and 35 °C, and with the FPA integration time of 0.1 ms. The noise was calculated as the standard deviation of the signal at the output of a unit cell over 20 frames. The NEDT was then calculated as

$$\text{NETD} = \frac{T_2 - T_1}{\text{SNR}},$$

where SNR = $(V_2 - V_1)$/noise, and T_2 and T_1 are, respectively, the higher (35 °C) and the lower (25 °C) background temperatures.The average NEDT of the VLWIR FPA was 53.5 mK, and the minimum was 21.4 mK.

4. Conclusions

In summary, an optimized strain balance process was usedfor controlling the MBE growth parameters for VLWIR wafers with high-quality materials. Then, the FPA was fabricated in a standard process. After hybridisation with ROICs, the fabrication of the FPAwas completed after removing the GaSb substrate and antireflection (AR) coating. Finally, an InAs/GaSbtype-II FPA with a 50% cutoff wavelength of 15.2 μm was obtained, demonstrating an excellent performance in the VLWIR range of wavelengths. The peak QE and the peak specific detectivity were 25.74% and 5.89×10^{10} cm·Hz$^{1/2}$·W^{-1}, respectively. The operability and the uniformity of responsivity were 89% and 83.17%, respectively. The average NETD was 53.5 mK.

References

[1] Esaki L and Tsu R 1970 *IBM J. Res. Dev.* **14** 61
[2] Johnson J L, Samoska L A, Gossard A C, Merz J L, Jack M D, Chapman G R, Baumgratz B A, Kosai K and Johnson S M 1996 *J. Appl. Phys.* **80** 1116
[3] Mohseni H, Tahraoui A, Wojkowski J, Razeghi M, Brown G J, Mitchel W C and Park Y S 2000 *Appl. Phys. Lett.* **77** 1572
[4] Wei Y J and Razeghi M 2004 *Phys. Rev. B* **69** 085316
[5] Nguyen B M, Chen G X, Hoang M A and Razeghi M 2011 *IEEE J. Quantum Electron.* **47** 686

[6] Bogdanov S, Nguyen B M, Hoang A M and Razeghi M 2011 *Appl. Phys. Lett.* **98** 183501
[7] Hood A, Delaunay P Y, Hoffman D, Nguyen B M, Wei Y J, Razeghi M and Nathan V 2007 *Appl. Phys. Lett.* **90** 233513
[8] Delaunay P Y, Nguyen B M, Hoffman D, Huang E K and Razeghi M 2009 *IEEE J. Quantum Electron.* **45** 157
[9] Wang G W, Xiang W, Xu Y Q, Zhang L, Peng Z Y, Lü Y Q, Si J J, Wang J, Xing J L, Ren Z W and Niu Z C 2013 *J. Semicond.* **34** 114012
[10] Razeghi M, Nguyen B M, Hoffman D, Delaunay P Y, Huang E K, Tidrow M and Nathan V 2008 *Proc. SPIE* **7082** 708204
[11] Hood A, Hoffman D, Nguyen B M, Delaunay P Y, Michel E and Razeghi M 2006 *Appl. Phys. Lett.* **89** 093506
[12] Mou S, Li J V and Chuang S L 2009 *IEEE IEEE J. Quantum Electron.* **45** 737
[13] Jiang D W, Guo F Y, Xiang W, Hao H Y, Wang G W, Xu Y Q, Yu Q J, Niu Z C and Zhao L C 2014 *Proc. SPIE* **9300** 93001L
[14] Nguyen B M, Razeghi M, Nathan V and Brown G J 2007 *Proc. SPIE* **6479** 64790S
[15] Hoffman D, Nguyen B M, Huang E K, Delaunay P Y, Razeghi M, Tidrow M Z and Pellegrino J 2008 *Appl. Phys. Lett.* **93** 031107
[16] Nguyen B M, Hoffman D, Delaunay P Y and Razeghi M 2007 *Appl. Phys. Lett.* **91** 163511
[17] Jiang D W, Xiang W, Guo F Y, Hao H Y, Han X, Li X C, Wang G W, Xu Y Q, Yu Q J and Niu Z C 2016 *Appl. Phys. Lett.* **108** 121110
[18] Hao H Y, Wang G W, Xiang W, Han X, Xu Y Q, Liao Y P, Zhang Y, Ren Z W, Ni H Q, He Z H and Niu Z C 2015 *Infrared Phys. Technol.* **72** 276
[19] Kutty M N, Plis E, Khoshakhlagh A, Myers S, Gautam N, Smolev S, Sharma Y D, Dawson R, Krishna S, Lee S J and Noh S K 2010 *J. Electron. Mater.* **39** 2203
[20] Hood A, Hoffman D, Nguyen B M, Delaunay P Y, Michel E and Razeghi M 2006 *Appl. Phys. Lett.* **89** 093506
[21] Miura K, Machinaga K, Balasekaran S, Kawahara T, Migita M, Inada H, Iguchi Y, Sakai M, Murooka J, Katayama H and Kimata M 2016 *Proc. SPIE* **9819** 98190V